Draft version October 16, 2022
Typeset using LATEX preprint style in AASTeX631

1

Properties of Flare-Imminent versus Flare-Quiet Active Regions from the Chromosphere through the Corona I: Introduction of the AIA Active Region Patches (AARPs)

Karin Dissauer, 1 K.D. Leka, 1,2 and Eric L. Wagner 1

<sup>1</sup>NorthWest Research Associates, 3380 Mitchell Lane, Boulder, CO 80301 USA <sup>2</sup>Institute for Space-Earth Environmental Research, Nagoya University, Furo-cho Chikusa-ku, Nagoya, Aichi 464-8601 JAPAN

(Received; Revised; Accepted)

Submitted to ApJ

#### ABSTRACT

We begin here a series of papers examining the chromospheric and coronal properties 10 of solar active regions. This first paper describes an extensive dataset of images from the 12 Atmospheric Imaging Assembly on the Solar Dynamics Observatory curated for large-13 sample analysis of this topic. Based on (and constructed to coordinate with) the "Active 14 Region Patches" as identified by the pipeline data analysis system for the Helioseismic 15 and Magnetic Imager (HMI) on the same mission, the "HARPs"), the "AIA Active 16 Region Patches" (AARPs), described herein, comprise an unbiased multi-wavelength 17 set of FITS files downsampled spatially only by way of HARP-centered patch extrac-18 tions (full spatial sampling is retained), and downsampled in the temporal domain but 19 still able to describe both short-lived kinematics and longer-term trends. The AARPs 20 database enables physics-informed parametrization and analysis using Nonparametric 21 Discriminant Analysis in Paper II of this series, and is validated for analysis using Dif-22 ferential Emission Measure techniques. The AARP dataset presently covers mid-2010 23 through December 2018, is ≈9Tb in size, and available through the Solar Data Analysis 24 Center (Dissauer et al. 2022b).

Keywords: methods: statistical – Sun: flares – Sun: corona – Sun: chromosphere

#### 1. INTRODUCTION

Coronal magnetic topology, energetics, and dynamics are all believed to play key roles in triggering, powering, enabling energetic events. However, large-sample studies of active regions that

Corresponding author: Karin Dissauer Corresponding author: K.D. Leka

dissauer@nwra.com

leka@nwra.com

27

28

34

35

search for clues as to solar energetic event productivity have long focused on characterizing pho-30 tospheric active region complexity through the analysis of continuum-image and magnetic field 31 data, and the subsequent association of resulting descriptors with flare activity (Sawyer et al. 1986; 32 Zirin & Liggett 1987; McIntosh 1990; Bornmann & Shaw 1994; McAteer et al. 2005; Leka & Barnes 2007; Kontogiannis et al. 2019; Leka et al. 2018; Al-Ghraibah et al. 2015; Korsós et al. 2014). In addition to descriptors based on the morphology of white-light images and the spatial distribution and character of the magnetic fields, such as the Zurich sunspot classification system, photospheric 36 analysis of solar active region flare productivity has also included plasma velocity and helicity pat-37 terns (Welsch et al. 2009; Park et al. 2018, 2021), wavelet and fractal analysis of photospheric images 38 (Abramenko 2005; McAteer et al. 2005; Georgoulis 2012; Al-Ghraibah et al. 2015), and inferred sub-39 surface plasma flows (Komm et al. 2011; Braun 2016).

The focus on photospheric magnetic fields and the drivers of their evolution makes physical sense, 40 as these are ultimately the source of energy to power solar energetic events. The physical interpreta-42 tion of the state of the photosphere for flare-productive active regions includes highly non-potential 43 magnetic fields that indicate stored magnetic energy, strong electric current systems and spatial gra-44 dients that provide pathways for magnetic reconnection, and emerging flux episodes that can desta-45 bilize the system (e.g. Zirin & Tanaka 1973; Krall et al. 1982; Hagyard et al. 1984; Canfield et al. 46 1975; Wang et al. 1996; Smith et al. 1996), (see also Leka & Barnes 2003a, 2007, and references 47 therein). These quantitatively interpretable characteristics provide the physics-based insight that 48 can then guide or constrain numerical modeling and further understanding (recent examples in-49 clude Threlfall et al. 2017). We intentionally cite some of the originating literature to highlight 50 these physics-inspired investigations that led to e.g., the Space-Weather HMI Active Region Patch 51 ("SHARP" Bobra et al. 2014) parameters currently published as meta-data physical summaries of so-52 lar magnetic complexes as a data product from the Solar Dynamics Observatory (SDO Pesnell et al. 53 2012) Helioseisemic and Magnetic Imager (HMI Scherrer et al. 2012; Schou et al. 2012; Centeno et al. 54 2014; Hoeksema et al. 2014).

In this series of papers we begin to do the same, quantitatively, for the chromosphere, transition region, and corona. The upper layers of the atmosphere are driven by, and respond to the pho-57 tospheric drivers. Case-studies of the pre-event chromosphere, transition region and corona have 58 shown evidence of specific pre-event energization and kinematics, starting with enhanced Hydrogen 59 Balmer-series "Hα" emission in flare-imminent active regions (Sawyer et al. 1986; Zirin & Marquette 60 1991), an increase in chromospheric non-thermal velocities and high blueshifts (Cho et al. 2016; 61 Harra et al. 2013; Woods et al. 2017; Seki et al. 2017), very localized chromospheric heating (Li et al. 62 2005; Bamba et al. 2014). Coronal brightness and morphological signals include the energization and 63 increased dynamic behavior of EUV structures ("crinkles"; Sterling & Moore 2001; Joshi et al. 2011; 64 Sterling et al. 2011; Imada et al. 2014, and references therein), and coronal dimmings (Imada et al. 65 2014; Zhang et al. 2017; Qiu & Cheng 2017) in the hours prior to energetic events.

Large-sample studies of the corona that relate its physical state to energetic-event productivity 67 have generally focused on modeling the coronal magnetic field and observationally inferring relevant 68 topological characteristics, often for coronal mass ejections (*e.g.* Barnes 2007; Barnes & Leka 2006; 69 Georgoulis & Rust 2007; Kusano et al. 2020) (although see Aggarwal et al. 2018, regarding filament 70 dynamics and eruptivity).

Thus far, investigations using the large-sample data available from the SDO Atmospheric Imaging 72 Assembly (AIA Lemen et al. 2012) in the context of energetic events have been carried out with a 73 primary goal of forecasting, rather than physical understanding. To achieve this expressed objective, 74 machine-learning tools have been invoked (Nishizuka et al. 2017; Jonas et al. 2018; Alipour et al. 75 2019), although these routinely subject the AIA data to significant degradation by spatial binning, 76 which hampers the ability to discern any small-scale processes. The outcomes have focused on skill 77 scores rather than physical interpretation, as "interpretable machine-learning" approaches have yet 78 to be widely implemented in this context. In other words, on many levels, information about the 79 physics of the corona has been lost or not pursued.

We focus here on the need to move away from case studies and toward the scientific objective of quantitatively characterizing the behavior of the chromosphere and corona using physically-82 meaningful analysis. We ask parallel questions about the chromosphere and corona as were posed 83 in previous works that centered on the photosphere (Leka & Barnes 2003a,b; Barnes & Leka 2006; 84 Leka & Barnes 2007): what are the broad physical differences between "flare-imminent" and "not-85 flareimminent" active regions? For the photosphere, we focused on descriptors of the vector magnetic 86 field and parametrizations that quantify, for example, the free magnetic energy available for energetic 87 events. For the present objectives, we focus on both high-frequency kinematic analysis indicative of 88 small-scale reconnection activity, and the hours-long trends in the brightness distributions indica-89 tive of growth, decay, or changing temperature distribution, or increasing or decreasing levels of 90 small-scale activity. We design the AARP database to address these objectives with a statistically-91 significant sample. As such, while we are not actively focusing on flare "prediction" per se, the results 92 of these investigations may inform those activities eventually, we propose that the AARP database 93 is designed such that it is appropriate for other, very different, scientific objectives, as well.

In this first paper of the series, we describe the data preparation for, and full description of, the
Ala Active Region Patch extractions (AARPs; Dissauer et al. 2022b, see Section 2). We present
global, cycle-scale trends across wavelengths in Section 3, plus some additional analysis aimed to 97
motivate community use of the AARP dataset. We leave the full discussion of physics-informed 98
parametrization and results from Nonparametric Discriminant Analysis to Leka et al. (Paper II; 99
2022), and of a statistical analysis of the temperature and density of flare-imminent regions using
Differential Emission Measure tools to Dissauer et al. (Paper III; 2022a).

## 2. THE AIA ACTIVE REGION PATCH (AARP) DATABASE

In this section we describe the AIA Active Region Patch (AARP) Database and its construction (see Figure 1). The data cubes were designed to make available a statistically significant sample of 104 solar active region coronal and chromospheric imaging data with a database of tenable size (noting 105 that the full-disk full-cadence AIA dataset for our target period is over 25Pb). The resulting cubes 106 are the basis for subsequent analysis (e.g. Leka et al. 2018) and are available to the community 107 (Dissauer et al. 2022b).

101

In the present incarnation, we specifically select the cadence and duration of the cubes to match those we have produced for photospheric active region investigations using the vector-field data from 110 HMI (Leka et al. 2018); future studies may require different such particulars. The infrastructure to 111 produce the present dataset as well as others with different such options is available (Dissauer et al. 112 2022b), although it presently relies on specific data access and architecture (see Appendix B, C). Not

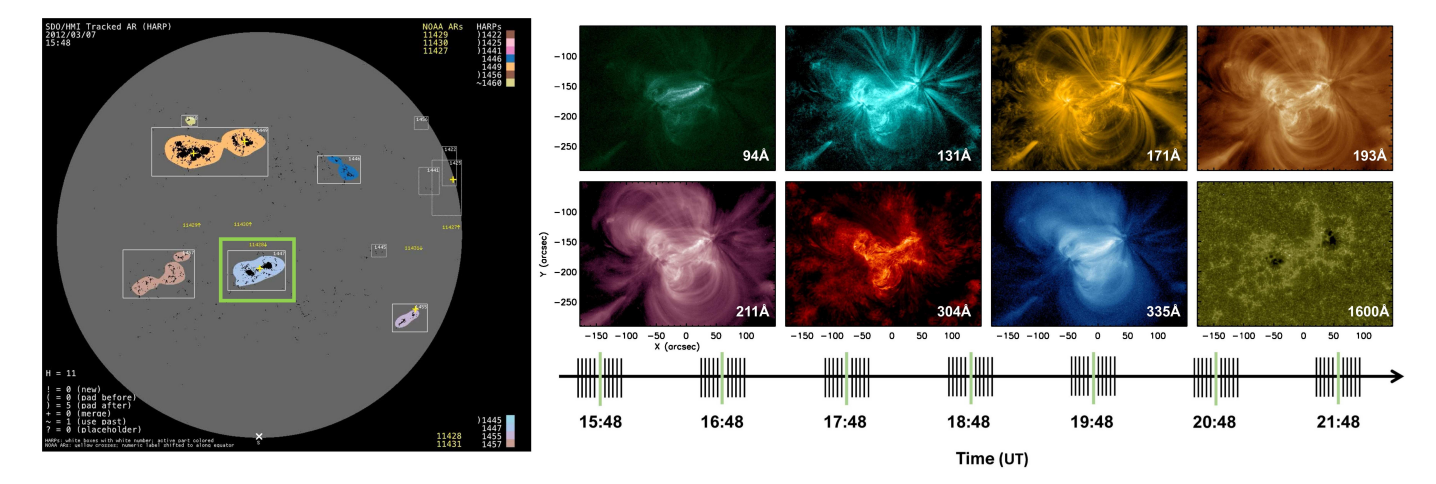


Figure 1. Overview of the AARP extraction and down-sampling in both spatial and temporal domains, for HARP/AARP 1447 on March 07, 2012. The AARP field-of-view is based on the HARP box (highlighted by the green boundary in the left panel; see Section 2.2). In the temporal domain, 11 images (right panel) per hour (see time line at the bottom) over the course of 1/4 of each day are extracted for 8 different (E)UV wavelengths (all but 1700Å; panels in upper/right).

everyone in the community has access to the hardware and software resources required to produce the
AARP dataset; we hope it will be of use to the community as a curated, ready-for-analysis resource. 115
The HMI Active Region Patch ("HARP" Hoeksema et al. 2014; Bobra et al. 2014) definitions are 116
used for the active-region identification system, and we intentionally include all HARPs. We do not
down-select at the active-region level, either for size or activity. HARP designations are based on 118
concentrations of magnetic activity, and the low-activity, small concentrations statistically dominate. 119
As such, we avoid imposing a bias for later analysis, although any comparison of (for example) active 120
vs. less-active regions must statistically account for the uneven sample sizes.

2.1. *AIA Data* 

The AARP database comprises coronal- and chromospheric time-series patches that are extracted 123 from the full-cadence full-size data of the Atmospheric Imaging Assembly (AIA; Lemen et al. 2012) on 124 board NASA's Solar Dynamics Observatory (SDO; Pesnell et al. 2012). AIA obtains 4096²-pixel full-125 disk coronal and chromospheric images at 1.5" spatial resolution, sampled at 0.6" through multiple 126 extreme-ultraviolet filter bands at [94, 131, 171, 193, 211, 304, 335] A with a 12 s cadence, and full-127 disk photospheric images at ultraviolet [1600, 1700] A with a 24s cadence. We embarked on this 128 project to avoid copying *all* of the data, instead focusing on active-regions specifically for the first 129 "down-selection" operation for the final database. However, that still required handling a significant 130 amount of AIA data.

NWRA employs the Joint Science Operations Center ("JSOC") "NetDRMS" (Network Data Record Management System) / "RemoteSUMS"(Storage Unit Management System) system to be able to 133 essentially mimic the availability of SDO (and other) data in a manner directly analogous to the host 134 institution, Stanford University. Large data transfers are handled through the "JSOC Mirroring Dae-135 mon" (see Appendix B). The AIA meta-data reside in the aia.lev1 euv 12s and aia.lev1 uv 24s 136 series, while the images reside in the aia.lev1 series within the NetDRMS/RemoteSUMS system 137 (the aia.lev1 series is largely transparent for data transfers through, e.g., the JSOC "LookData"

facility). Details of setting up automatic targeted Java Mirroring Daemon (JMD) transfers and per- $_{139}$  forming the extractions are provided in Appendix B. For small numbers of HARPs or customized  $_{140}$  extractions, the SolarSoft ssw cutout service.pro (Freeland & Handy 1998) is recommended to be used, however as described in Appendix C, it was not the correct tool by which to develop the AARP database.

138

141

142

143

157

158

159

160

173

## 2.2. Down-Select in the Spatial Domain: Extracting the Active Region Patches

This dataset is created to address the almost untenable requirements of large-sample coronal studies. 145 The "AIA Active Region patches" (AARPs) are first and foremost a down-selection in the spatial 146 domain, providing sub-area extractions from the full-disk AIA image data that rely on the HMI 147 Active Region Patches (HARPs; Hoeksema et al. 2014) metadata (hmi.Mharp 720s series) for target 148 selection, pointing, and field-of-view (FOV) definition.

Because coronal structures extend in height from the solar surface, the extraction box is modified  $_{150}$  from the original HARP FOV to accommodate this projection effect both when a region is viewed  $_{151}$  face-on but also as it is viewed away from disk center (see Figure 2). Hence, we expand the original  $_{152}$  HARP FOV by 20% in both x-, y- directions, limited to a maximum expansion of  $_{25}$  to avoid  $_{153}$  unwieldy increases in already-large HARPs. Additionally, we augment with an expansion towards  $_{154}$  the East or the West  $_{8x}$  depending on the position of the HARP center with respect to the central  $_{155}$  meridian in the form of

$$x_{ex} = x_{cen}[°]/90° \cdot 50″,$$
 (1)

where  $x_{cen}$  is the center of the HARP in degrees. This expansion is limited to a maximum extension of 50" and is done to accommodate the additional extension of loops viewed from the side as a region approaches the solar limb. Figure 2 shows two examples, a disk-center and a near-limb target, comparing the original HARP (cyan box) and resulting AARP fields of view. While loop 161 tops originating from the target active region may still be cut off, the primary science this dataset 162 is designed for concerns relative (vs. absolute) changes in AR behavior, and since all regions are 163 treated consistently, this should impose no statistical concerns. In addition, automatically defining 164 an optimal FOV for each individual active region is challenged by (1) AARPs frequently being in 165 close proximity during periods of high activity, and (2) an optically-thin corona, such that there is 166 arguably no optimal way to automatically disentangle all visible loops, their source active regions, 167 and still ensure their tops are always included and correctly assigned.

All HARPs are included regardless of flaring activity levels, size of active regions, or observing 169 angle. The originating HARP bounding-box information is used for the central-time (the "XX:48") 170 image targets. The extracted higher-cadence 11-image timeseries is co-aligned between the (nearly co-171 temporal) wavelengths and the central-time image using differential rotation to allow for Differential 172 Emission Measure (DEM) analysis (Figure 3; see also Appendix E) but no further tracking is needed.

#### 2.3. Down-selecting in the Temporal Domain

To reduce the data load while preserving the scientific requirements of the research performed in Paper II and further projects, we down-sample the data in the temporal domain. The native 176 cadence for AIA EUV images is 12 s, and for the UV images it is 24 s. The AIA Automatic Exposure 177 Control (AEC) system is an observation mode designed to avoid image saturation during solar flares. 178 When the AEC system is invoked, the AEC-regulated images for the EUV data are inter-leaved with

181

182

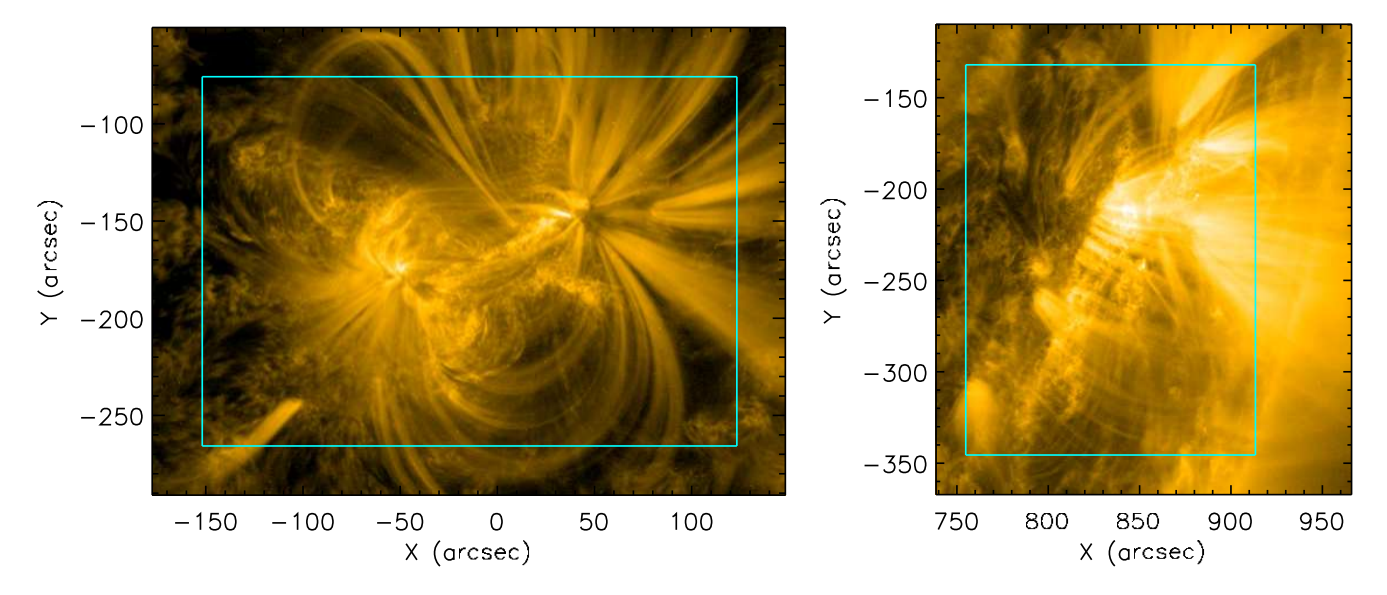


Figure 2. Two examples of the same AARP in 171Å illustrating the field-of-view expansions as a function of location on the disk and HARP dimensions. Symmetrical (left) extensions are used near disk center, and asymmetric extensions to include coronal loops are employed as regions approach the limbs, e.g. West (right) limbs. The cyan box marks the original HARP field-of-view. Left: AARP #1447 (NOAA AR 11428) 2012.03.07 15:48 UT; Right: AARP #1447 (NOAA AR 11428), 2012.03.12 15:48 UT.

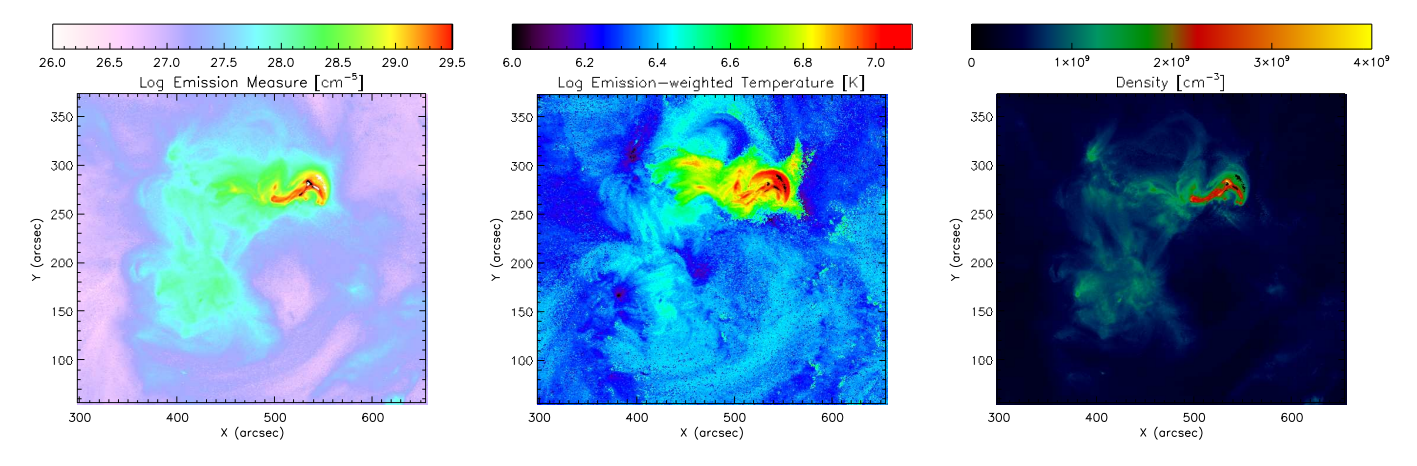


Figure 3. Analysis using Differential Emission Measure (Cheung et al. 2015) for HARP/AARP 3894 (NOAA ARS 12017 & 12018) on March 29, 2014 at 17:42:01 UT. Left: emission measure map (log-scale), Middle: emission-weighted temperature map (log-scale), Right: density map.

normal-exposure (possibly saturated) images, reducing the effective cadence for consistent-exposure 180 EUV data to 24s. Native images in data numbers ("DN") or counts can be normalized by the exposure time to obtain consistent per-pixel count rate-based images. For reasons described below, however, we decided to avoid the AEC-regulated images and sample the AIA images at a 72 s cadence.

The image parametrization for the statistical analysis in Paper II and later work uses moment 184 analysis to describe the coronal and chromospheric behavior. During flare times, even for small 185 flares, the higher moments jump dramatically – as expected in the presence of localized yet high-186 magnitude brightness changes (Figure 4, left four panels). Our scientific focus is not, generally, the

191

192

223

flaring plasma itself but the broad active region behavior. Avoiding the AEC images allows for times 188 of flares to be included with less dramatic impact to the moment analysis. Additionally, the shorter 189 exposures during flaring times lead to lower signal/noise ratios (SNR) for the larger active region 190 areas (Figure 4, right panels). Since these regions are our focus, ensuring a consistent SNR is key. Finally, given the format of the AARP FITS files (see Appendix A), avoiding the AEC data allows a simplified metadata format, as the exposure time is consistent for a particular wavelength.

When working with running-difference images, central to our analysis approaches, the native ca- $_{194}$  dence presents two challenges: (1) for consistent-exposure sequential images the resulting SNR was  $_{195}$  very low, and (2) when sequential images had varying exposure times, the resulting variation in the  $_{196}$  images' SNR contributed to even higher noise in the running-difference images. While the running- $_{197}$  difference magnitudes increase as  $\Delta t$ , one must also balance this increase in SNR with the ability to  $_{198}$  evaluate and interpret the resulting images. Experimentation indicated that the full time resolution  $_{199}$  is unnecessary to capture the short-lived brightenings and kinematics that we wish to examine.

A coarser 72 s cadence for the AARP "high-cadence" bursts of images thus provides a good balance 201 of consistent and acceptable SNR and dataset volume reduction. Selecting a 72 s cadence is also a 202 "common factor" between the EUV and UV native sampling, allowing for the dataset to sample the 203 different atmospheric layers at the same cadence.

The evolution of the corona over multiple hours is of high interest here. An interval covering ≈ 6 hr is motivated by numerical models of pre-event evolution and trigger formation (Ishiguro & Kusano 206 205 2017; Inoue et al. 2018), and provides sufficient data from which to quantify overall evolutionary 207 trends within an active region. Still, 72s sampling over 6 hr is a large data load. Hence we further 208 down-select to ≈ 13 min of images at the 72 s cadence, centered hourly 15:48 – 21:48 UT (seven hourly 209 "bursts" of images, over six hours, inclusive). The choice of timing is driven by an already-developed 210 of HMI vector-field time-series extracted data-set (Leka et al. 2018). Centering the data on the 211 "XX:48" times was necessary to avoid those HMI data affected by calibration sequences (taken at 212 00:00 and 18:00 TAI, see Hoeksema et al. (2014)). Those studies also had a scientific requirement 213 to minimize the statistical impacts on time-series analysis that were solely due to the spacecraft 214 orbital velocity-induced artifacts (Hoeksema et al. 2014). Finally, we chose 11 images covering 13 m 215 to effectively match the time period over which the input spectra are averaged for the hmi.B 720s 216 series magnetograms. In this sense, we sample the upper atmosphere on a cadence appropriate to 217 its physics (reconnection, heating, flows) but carefully pair the extractions to their arguably slower-218 evolving photospheric driver, at least at the HMI spatial resolution.

Thus, in summary, with the AARPs dataset the detailed behavior of the lower solar atmosphere is sampled at a fair cadence (72 s) for 13 m every hour, repeatedly over a quarter of a day for a full  $_{221}$  8.5 yr (06/2010 – 12/2018) over which we can query about active region trends using a large-sample  $_{222}$  approach that enables robust statistical analysis.

## 2.4. Final Data-Cube Preparation

All AIA data are processed through the SolarSoft (Freeland & Handy 1998) routine aia prep.pro and a correction to account for time-dependent degradation of the instrument was applied using the 226 following form:

$$\frac{A_{eff}(t_{obs})}{A_{eff}(t_0)} 1 + p_1 \delta t + p_2 \delta t^2 + p_3 \delta t^3 , \qquad (2)$$

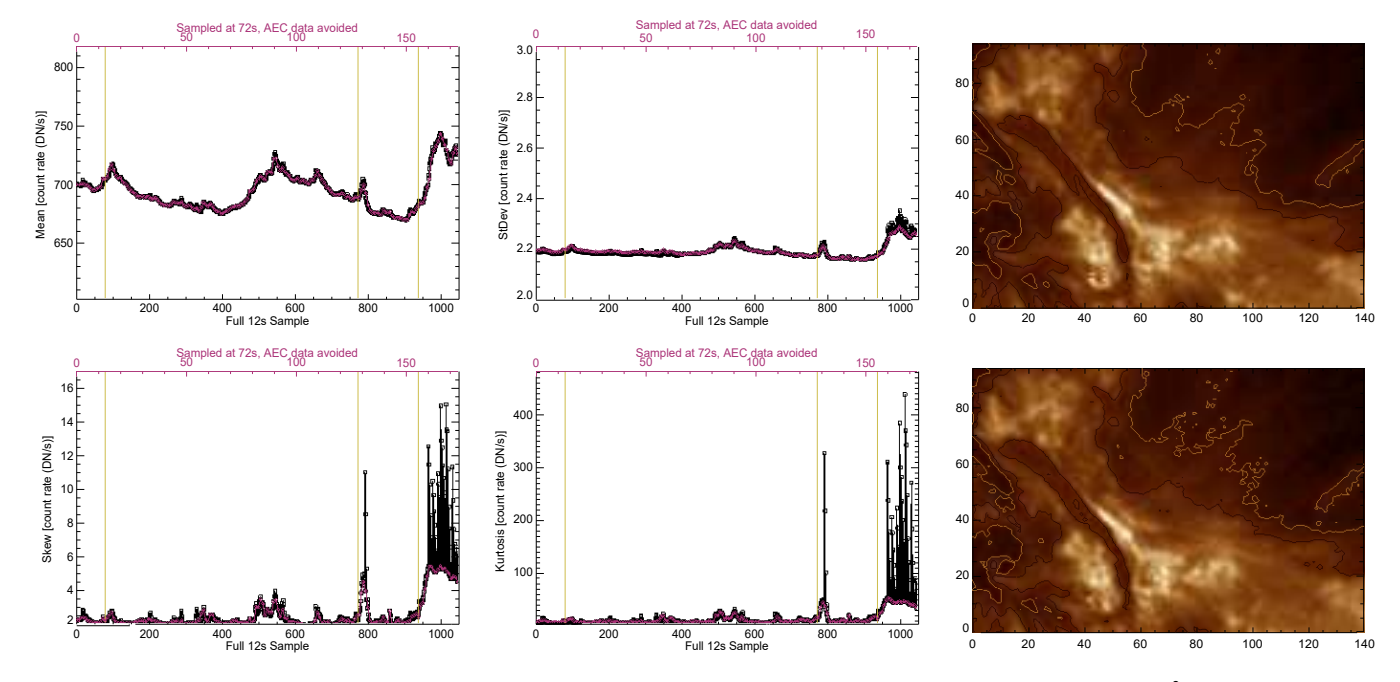


Figure 4. Example parameter curves from AARP #750 (NOAA AR #11261) for 193A on 2011.08.03 00:00UT – 03:30 UT; the start of a sub-flare at 00:18 UT, a C1.2 at 02:35 UT and the M1.1 flare at 03:08 UT are indicated by dashed vertical lines. The bottom x-axis is an image index for the original 12 s sampling (black), the top x-axis are the indicies for the 72 s sampling (red) used for the AARPs that naturally avoided the AEC-triggered images. All data were exposure-normalized. Left four panels show the four moments of the images, as indicated. Right two panels show a small sub-area of the full AARP field of view that includes a small filament and nearby loop-bottoms (top/right of the images), but avoids the M1.1 flare-emission area, for two consecutive 12 s-sampled images, Top: normal 2s exposure, Bottom: 0.43 s exposure, when AEC-mode was invoked. Light/Dark contours indicate the [2, 3] σ signal/noise levels, with the noise level determined by the most-probable value of low-signal parts of the image.

where  $A_{eff}(t_{obs})$  is the effective area calculated at the calibration epoch for  $t_{obs}$ ,  $A_{eff}(t_0)$  is the effective 229 area at the first calibration epoch (i.e. at launch), p1, p2, p3 are the interpolation coefficients for the  $t_{obs}$  epoch, and  $\delta t$  is the difference between the start time of the epoch and  $t_{obs}$  (Barnes et al. 2020).

All wavelengths and imaging data centered at each hour are coaligned and differentially rotated to 2322 the central time step (usually \*\*:48 UT) using drot map.pro. The pre-processed output data are therefore ready for running-difference analysis and Differential Emission Measure (DEM) analysis 234 (see Appendix E). Full FITS headers are generated with wavelength, HARP number, NOAA Active Region (AR) number (from the relevant keywords in the hmi.MHarp 720s series). The seven sets of hourly image sets are saved as extensions each with its own header recording times, number 237 of valid images, and detailed pointing information as well as additional keywords imported from 238 the hmi.MHarp 720s series such as LAT FWT, LON FWT and the World Coordinate System (WCS; Thompson 2006) keywords for the target 720s-based mid-time. Appendix A contains examples of these AARP fits headers.

The final data product thus comprises a set of eight FITS files, one for each wavelength (by default: 242 94, 131, 171, 193, 211, 304, 335, and 1600 A), for each HARP covering six hours inclusive (seven 243 hourly samples 15:48 – 21:48 UT) of 13 minutes of data sampled at 72s, resulting in 11 images per

hour. The full dataset is summarized in Table 1, its archive size being only  $\approx 9.5$  Tb, in contrast to the size of the full-disk AIA dataset for this period which is  $\approx 25$  Pb. The power of the dataset is its large, yet tenable sample size, designed to enable unbiased statistical analysis on spatially native-247 resolution images. We next present some topics for which models or case-studies may now be tested 248 on a statistically significant, cycle-covering sample.

Table 1. AARP Data Set Summary

Date Range	HARP Range	NOAA AR Range	Total Number of Samples	Archive Size
06/2010 - 12/2018	36 – 7331	11073 – 12731	256,976	≈ 9.5 TB

### 3. ANALYSIS & RESULTS

We present here a brief analysis to highlight the breadth of physics investigations that could be performed using the AARP database. We do not discuss flare- or event-related studies in depth, deferring this topic to Paper II (although see Section 3.4).

# 3.1. Active Region Coronal Behavior with Solar Cycle

With this extensive database we can begin to examine some subtleties of coronal behavior for 255 active regions as a function of solar cycle. Generally speaking the AARPs will not include significant 256 coronal hole areas, and thus will avoid that contamination and source of confusion with regards to 257 interpretation.

In Figure 5 we present density histograms of total emission in AARPs for two AIA bands over most of Solar Cycle 24, as well as the same presentation for the mean emission in the same bands. We focus on 171 Å that is sensitive to plasma at "quiet" coronal temperatures and transition region emission, and thus is often used to identify coronal magnetic structures such as coronal loops, and the 94 Å band that is sensitive to hot plasma (Lemen et al. 2012), but that can contain contributions from cooler lines within the bandpass (O'Dwyer et al. 2010; Warren et al. 2012; Del Zanna 2013).

The "total" emission ( $\Sigma(I_{\mathbb{B}})$ ) distribution tracks nicely with sunspot number, as expected, since it is an extensive parameter that scales with the size of the box, number of pixels, or more physically, the total amount of magnetic flux present. In both bands we see that the vast majority of AARPs have small total emission, a high density of points that itself tracks the sunspot number generally. In both bands there are also the less-frequent larger-total-emission regions whose distribution tracks the sunspot number even closer. None of this is unexpected.

What is interesting is that while for most "bumps" in total emission, *i.e.* those for which the eye <sup>271</sup> sees a good correlation with a "bump" in sunspot number, there is good correspondence between <sup>272</sup> the two passbands. However, there are apparently some large active regions for which a large total <sup>273</sup> 171 A is *not* matched with a correspondingly large total in 94 A (*e.g.* late 2010, late 2017, early 2018) <sup>274</sup> and *vice versa* (*e.g.* mid 2012, early 2015). Thus, while well correlated, the total emission displayed <sup>275</sup> in these two channels may not be uniquely correlated, which prompts the questions "why or why <sup>276</sup> not?" One immediate reason is the multi-thermal nature of both the ATA channels and active regions <sup>277</sup> themselves. Clearly this extensive dataset can begin to address the details of active region coronal <sup>278</sup> emission with, e.g., AR age, magnetic field morphology, and flaring history, and provide constraints

281

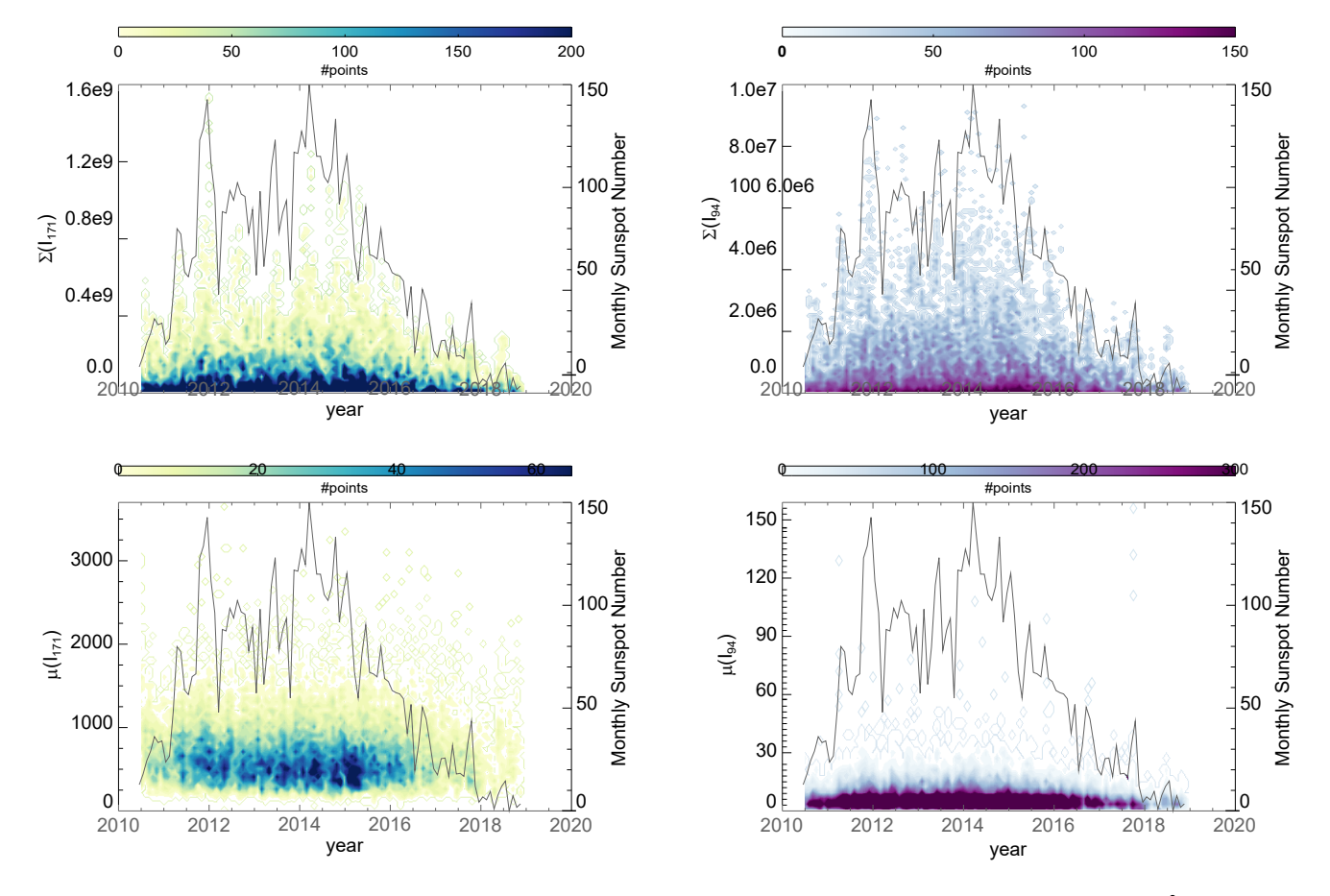
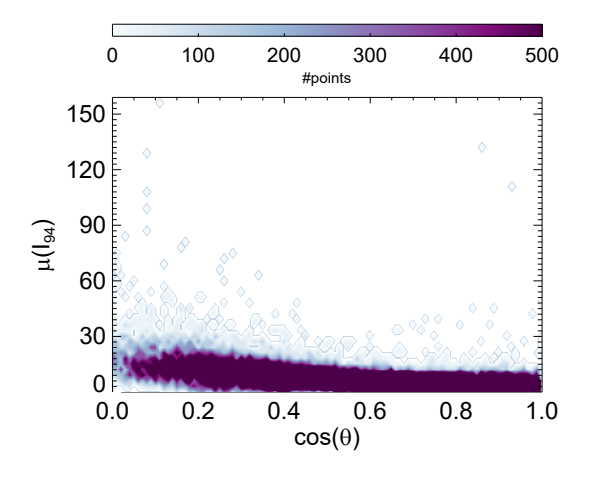


Figure 5. Top Row: Density histograms of the total emission of each AARP for 171A (left) and 94A (right) as a function of date, left axes. Also plotted is the monthly mean sunspot number from SILSO World Data Center (2010-2018), right axes. The density histograms do include the 'single-point' values as the lowest contour / lightest color. Bottom Row: Same presentation but for the mean emission (size-normalized) of the two bandpasses.

for modeling efforts both with regards to intra-filter expected emission and variations with solar 280 cycle. This is especially true since, as discussed in sections 2.4, Appendix E - the data are ready for not just hot-plasma isolation (Warren et al. 2012), but full DEM analysis.

The mean emission tells a slightly different story. Figure 5 shows that if there magnetic flux is  $_{283}$  present (as defined the HARPs and hence the AARPs), there is emission in  $171\,\text{A}$ , or  $\mu(l_{171})$   $\Omega$  0,  $_{284}$  essentially. The same is not quite as true for  $\mu(l_{94})$  where the majority of AARPs display a low or  $_{285}$  near-zero mean emission. This is consistent with  $\mu(l_{94})$  having sensitivity to hot coronal emission,  $_{286}$  which not all active regions contain (especially flare-quiet ones). However,  $\mu(l_{171})/\mu(l_{94})$  may not be  $_{287}$  perfectly constant with solar cycle. These simple findings are consistent with Schonfeld et al. (2017)'s  $_{288}$  sun-as-a-star investigation showing that the cool / quiet-Sun corona varied little over the first half of  $_{289}$  SC24 while the hot component varies strongly with the rise in solar activity. A thorough investigation  $_{290}$  using the AARP database could provide further physical constraints especially with respect to the  $_{291}$  AR-based contributions to the two components and possibly with regards to "terminator" analysis  $_{292}$  (Leamon et al. 2022).



313

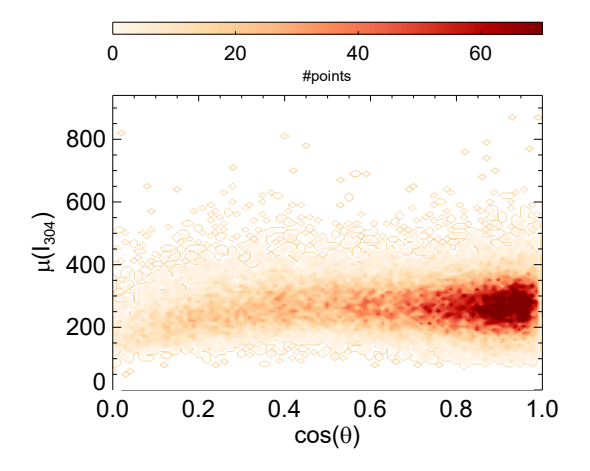


Figure 6. Density histograms of the area-averaged  $94\,\text{Å}$  emission (left) and  $304\,\text{Å}$  emission (right) as a function of observing angle. Shown are the results for all AARPs regardless of size or other selection criterion.

# 3.2. Active Region Coronal Behavior with Observing Angle

The coronal emission lines are generally optically thin. However, a few of the AIA bandpasses are 295 centered on, or include, optically thick emission (Golding et al. 2017). Additionally, when densities 296 become large such as during solar energetic events, some of the normally optically-thin lines in the 297 sampled bandpasses become optically thick (Thiemann et al. 2018). The differences in behavior can 298 be seen when the mean emission levels of different lines are presented according to their location 299 on the disk (Figure 6). The 94 A channel generally displays a small mean emission that is flat with 300  $\mu$  = cos( $\theta$ ) except at the very limb, where the optically-thin properties afford a propensity to integrate 301 over more emitting structures along the line-of-sight.

The He II 304 Å emission is optically thick but has challenging radiative transfer characteristics 303 (Golding et al. 2017), and thus expected to show a correlation with observing angle  $\cos(\theta)$  (decreasing 304 toward the limb). The density distribution of  $\mu(I_{304})$  (Figure 6, right) does show a slight turnover 305 beyond  $\mu = \cos(\theta) = 0.25$  or  $\theta = 75^{\circ}$  but it is extremely slight. There is no severe or obvious 306 attenuation with observing angle, but the behavior of He II 304 A emission in active regions may 307 not have yet been studied with large-sample data. There is the possibility of contamination within 308 the AIA filter by optically-thin emission that would mask the He II 304 A behavior, and it also 309 may be contaminated by the different behavior expected by different magnetic structures within the 310 AARP fields of view (Mango et al. 1978; Worden et al. 1999). The detailed behavior of the corona 311 as inferred from optically-thin dominated vs. optically-thick dominated AIA filters for active regions 312 can now, with the AARP database, be studied in detail with large-sample statistical analysis.

### 3.3. Coronal Behavior with Active Region Emergence / Decay

The relationships (in the spatial and temporal domains) between coronal emission and emerging 315 magnetic flux should provide insights into the energy transfer to the upper atmosphere from the 316 photosphere and below. Similarly, the relationships between coronal emission and decaying active 317 regions should elucidate the final transfer of magnetic energy out of the Sun and the dominant 318 dispersion and dissipative mechanisms at play. The AARPs provide the ability to examine these 319 processes by sampling regions at all sizes and stages of evolution with a curated, large-sample dataset.

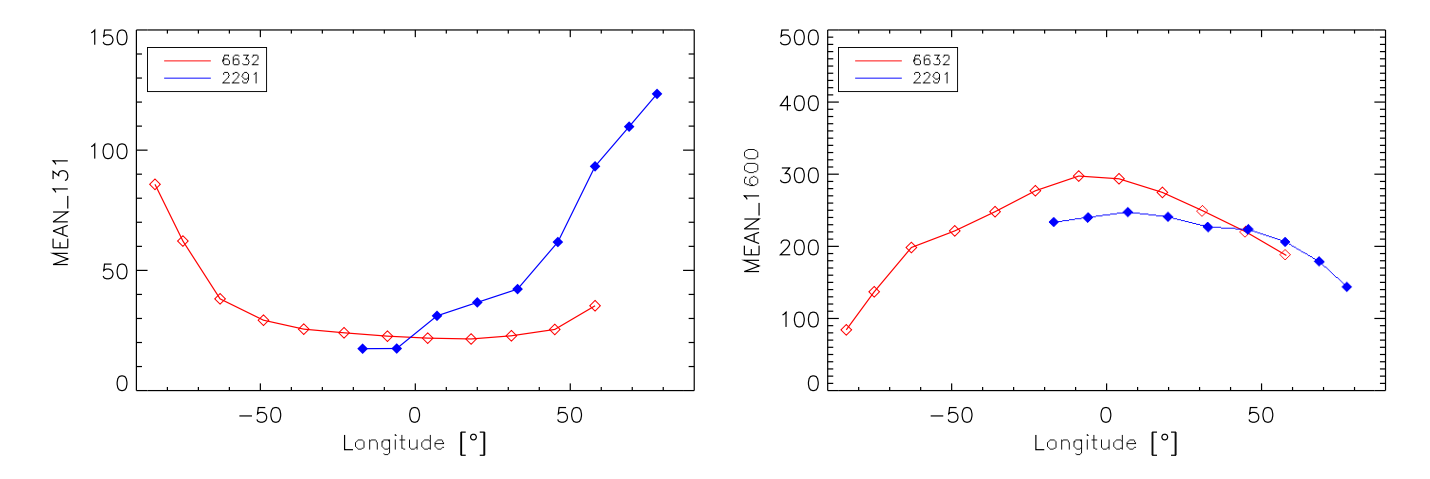


Figure 7. Two HARP/AARP regions and their mean emissions in two AIA filters. AARP 2291 grew rapidly starting near disk-center in 2012.12 to become NOAA AR 11631 and 11632. AARP 6632 (NOAA AR 12556, 2016.06) decays during disk passage. See text for discussion.

In Figure 7 we show the transition region/flaring plasma sensitive  $\mu(I_{131})$  and upper-photospheric  $_{321}$   $\mu(I_{1600})$  for two AARPs that are in significantly different stages of evolution as they traverse the  $_{322}$  disk. AARP 2291 underwent rapid growth starting near disk center and eventually became NOAA  $_{323}$  ARS 11631 and 11632. It displays a rapid growth in the mean intensity in the coronal Fe VIII,XXI  $_{324}$  131 A filter emission. AARP 6632 rotated on to the disk as NOAA AR 12556 and decayed to plage  $_{325}$  by disk-center. Its 131 A filter emission decays to essentially background. The comparison of the two  $_{326}$  regions in the  $\mu(I_{1600})$ , however, indicate that (as expected) this emission is optically thick (decreases  $_{327}$  systematically toward the limb) and is sensitive to the presence of plage rather than sunspots, with  $_{328}$  little difference between young and old plage.

Obviously we simply present a comparison here in order to encourage interest. We do not, for example, try to perform a larger-sample re-examination of the relationship between flux transport, 331 flux decay, and active region EUV radiance decay (Ugarte-Urra et al. 2017) but that is one study 332 the AARPs could confirm with larger-sample statistics. Other questions are ready for analysis: Are 333 there significant differences in coronal characteristics between old and new plage? Between emerging 334 regions that will become flare productive and those that will stay quiet?

# 3.4. Coronal Behavior with Activity Level

The AARP dataset was prepared specifically for a large-sample investigation into the coronal be-337 havior as related to flaring activity. We defer our study details and results to Paper II (Leka et al. 338 2022) but here present a preliminary example of the directions available for study with the AARP 339 dataset.

We note that indeed, the AARPs are not extracted according to the time of flares, meaning that they are *not* designed for super-posed epoch analysis (*e.g.* Reinard et al. 2010; Mason & Hoeksema 342 2010; Bobra & Couvidat 2015; Jonas et al. 2018). They are, however, extracted for quantitative 343 interpretable analysis and not flare prediction in & of itself, as have been many recent studies using 344 large samples of AIA image data (*e.g.* Nishizuka et al. 2017; Jonas et al. 2018; Alipour et al. 2019).

In Figure 8 we show both the "direct" (" $I_{193}$ ") and running-difference (" $\Delta I_{193}$ ") images, in the 193A  $_{346}^{\circ}$  band, for NOAA AR 11261 (HMI HARP 750, see Figure 4) on 2011.08.03. The quieter example is  $_{347}^{\circ}$  from the images centered at 21:48 UT, and the "active" example is taken from images centered at  $_{348}^{\circ}$  19:48 UT during a C8.5 flare. The two "direct" images look fairly similar, even during a flare, with a  $_{349}^{\circ}$  small localized brightening the only easily discernible difference. The running-difference images look  $_{350}^{\circ}$  very different. In the quiet example, there is a lot of small-scale fluctuation happening even outside  $_{351}^{\circ}$  the flare time. In the flare case, it is true that the saturated-emission area will show a lack of any  $_{352}^{\circ}$  dynamics, but do note that as the edges change, there are strong temporal gradients in this area.  $_{353}^{\circ}$  The expanding loops are also clearly visible in the running difference image.

The images look similar to the eye, as the flare was not very large, but the images are quantitatively  $_{355}$  different as summarized by the moments (mean  $\mu$ , standard deviation  $\sigma$ , skew  $\varsigma$  and kurtosis  $\kappa$ )  $_{356}$  presented in the table associated with Figure 8. In particular, the mean intensity at the two times  $_{357}$  is similar for both the direct and running-difference images (the latter both being fairly close to zero  $_{358}$  relative to the mean intensities) but the higher-order moments both for the direct and especially  $_{359}$  the running-difference are very different. Physically this implies enhanced localized brightening and  $_{360}$  kinematics on short timescales with little overall brightness enhancement or mean brightness increase  $_{361}$  as would indicate (for example) significant differences in active-region-scale heating or density between  $_{362}$  the two time periods.

#### 4. SUMMARY AND CONCLUSION

363

We present here the NWRA "AIA Active Region Patches" (AARP) Database (Dissauer et al. 2022b) that well-samples the temporal evolution of solar active regions as captured in the E/UV 366 with SDO/AIA over the majority of Solar Cycle 24 from 2010/06 – 2018/12. The current version of 367 the database includes daily, 7 hr samples of 13 minutes of images (centered hourly on "\*:48 UT" from 368 15:48 – 21:48 UT) targeting all magnetic patches identified by SDO/HMI, resulting in a total sample 369 size of 256,976 FITS files containing in total almost 20 Million individual SDO/AIA images. We show 370 a teaser of the analysis that could be performed using this dataset, including coronal behavior as 371 related to the solar cycle, to the emergence and decay of solar active regions, as well as center-to-limb 372 variations.

Crucially, the dataset is prepared with attention to quantitative analysis methodology. The AARPs  $_{374}$  dataset preserves the native spatial resolution of SDO/AIA (i.e.  $_{1.5}$ " sampled at  $_{0.6}$ "), in contrast  $_{375}$  to other studies that downsample the full-disk images to  $_{e.g.}$ ,  $_{512}$  ×  $_{512}$  (e.g. Galvez et al. 2019)  $_{376}$  or use solely an active region's total intensity or maximum intensity in a particular channel (e.g.  $_{377}$  Nishizuka et al. 2017). Keeping the full spatial resolution allows us to capture small-scale dynamics  $_{378}$  of the studied active regions (see e.g. Figure 8), which are otherwise lost due to binning.

However, we note that the dataset is (currently) limited to a selected time range (to match the NWRA database of HARP-based photospheric vector field timeseries data (Leka et al. 2018)) al-381 though with an extended field-of-view from the original defining HARP bounding box to capture 382 the projections of structures that extend in height. For our initial purpose of investigating unique 383 coronal and chromospheric characteristics of flare-imminent active regions, this is a valid approach 384 since both the short-term changes (over the course of 13 minutes every hour at a cadence of 72s) as 385 well as longer-term trends (7 hr of evolution per day per HARP) can be studied.

We stress that the AARP dataset is ready for machine-learning applications or any other largesample analysis. Importantly, it has been validated for Differential Emission Measure analysis (see

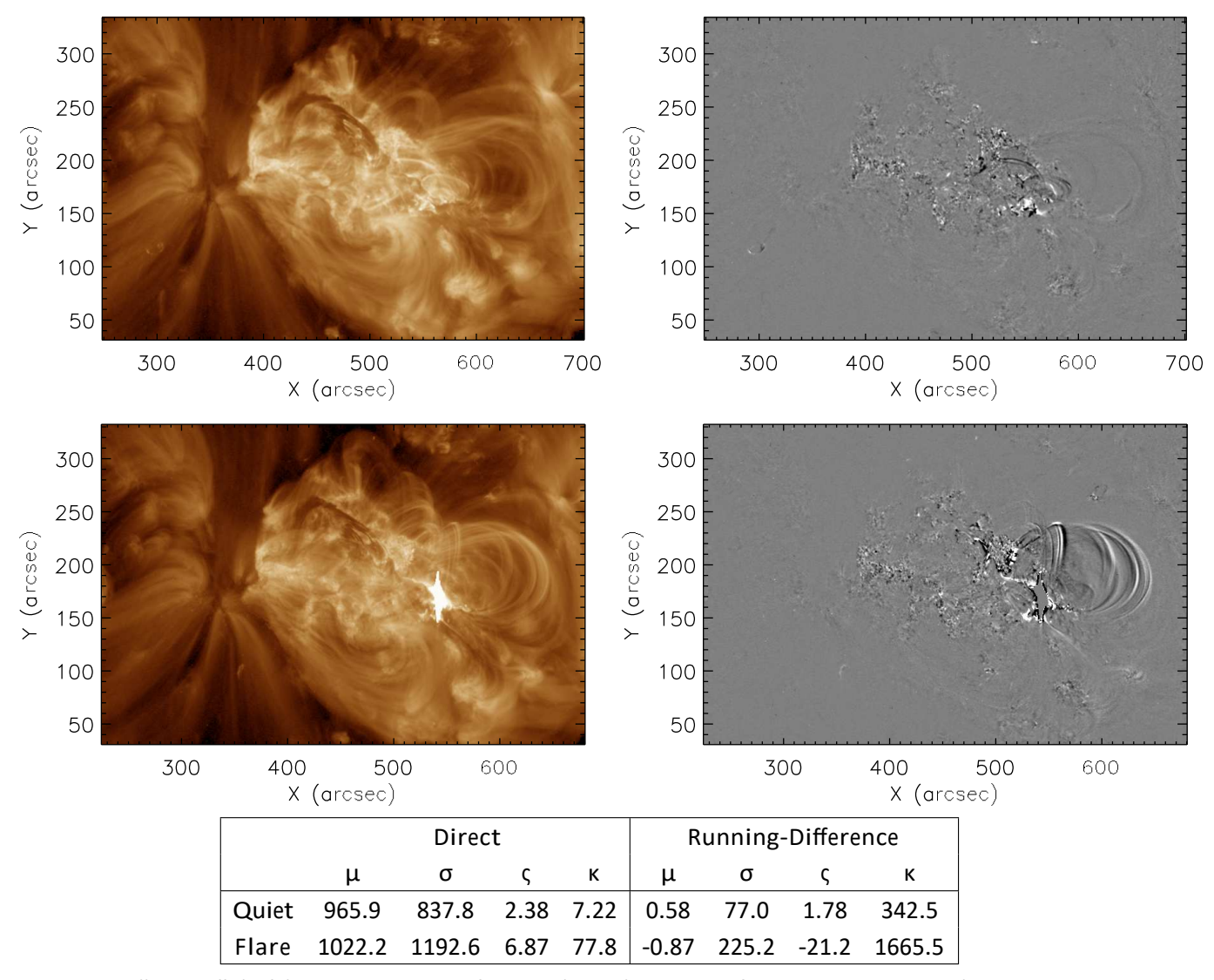


Figure 8. "Direct" (left) and running-difference (right) images of NOAA AR 11261 (HMI HARP 750, see Figure 4) on 2011.08.03 showing the differences between a quiet time (top, 21:46:50-21:45:38 UT) and during a small flare (bottom, 19:46:38-19:45:26 UT). Of note, the pairs of images are scaled the same, and while the flaring time does show a small patch of saturation since we avoid the AEC images, the pixels around the saturation area have extreme signals in the running-difference images as the saturated area changes with time.

Appendix E), which is a data product to be released in the near future. We note that this dataset could be easily expanded to include additional times sampled over each day, even at a different 390 cadence, such that both forecast-mode and superposed epoch mode analysis can be performed on every single flare that occurred since the start of the SDO mission. Although currently beyond the scope of this paper and not needed for the analysis presented in Paper II, such an expansion is quite feasible given the infrastructure NWRA has now developed.

The authors thank the referee for a thorough reading and insightful feedback that helped improve the paper. This work was made possible by funding from AFRL SBIR Phase-I contract FA9453-14-M-396 0170, (initial exploration), but primarily by NASA/GI Grant 80NSSC19K0285 with some additional 397 support from NASA/GI Grant 80NSSC21K0738 and NSF/AGS-ST Grant 2154653. We extend our sincere thanks to Sam Freeland for his patience and help with the ssw cutout service.pro chal-399 lenges.

407

400 APPENDIX

### A. THE AARP FITS FILE FORMAT

AARP FITS files contain in total eight extensions. The first extension, i.e. extension 0 is the primary header and contains no data. A sample primary header is given in Table 2. The primary header is be followed by seven image extensions that contain 11 images per extension, from 15:48–405 21:48 UT. An example for an image extension header is given in Table 3.

The FITS keyword values are either extracted from the original AIA keywords<sup>1</sup> or computed from the WCS coordinates upon field-of-view determination and extraction.

```
SIMPLE
                TNT
BITPIX
                LONG
                             <u>1</u>6
                                                                        'NUMBER OF DIMENSIONS'
'FITS FILE CONTAINS EXTENSIONS'
NAXIS
                LONG
                             0
EXTEND
                INT
INSTRUME
                STRING
                             'AIA'
                                                                         'Instrument name'
TELESCOP
                STRING
                             'SDO/AIA'
                                                                        '[angstrom] Wavelength'
'HMI Active Region Patch number'
'NOAA AR number that best matches this HARP'
WĀVĒLŇŤH
                             211
                LONG
HARPNUM
                LONG
                             377
NOAA_AR
                LONG
                             11158
                                                                         'Number of NOAA ARs matching this HARP (0 allowed)' List of NOAA ARs matching this HARP'
NOAA_NUM
                LONG
                             <sup>7</sup>11158'
NOAA_ARS
                STRING
                                                                        'Number of images in each extension'
'Total number of times in time series'
'Time of first observation in timeseries'
NSAMPS
                LONG
                             11
NTIMES
                LONG
T_START
                STRING
                             '2011.02.15_15:48:00_TAI'
T_STOP
TREC_00
                             '2011.02.15.21:48:00.TAI', '2011.02.15.15:48:00.TAI',
                                                                        'Time of last observation in time series'
                STRING
                                                                        'Extension #1
                STRING
                                                                                                  time<sup>-</sup>
                             '2011.02.15.16:48:00.TAI',
'2011.02.15.17:48:00.TAI',
'2011.02.15.18:48:00.TAI'
                                                                         'Extension #2
TREC_01
                STRING
                                                                                                  time'
TREC-02
TREC-03
                STRING
STRING
                                                                        Extension #3 Extension #4
                                                                                                  time,
                STRING
STRING
                             '2011.02.15_19:48:00_TAI',
'2011.02.15_20:48:00_TAI'
TREC_04
TREC_05
                                                                        'Extension #5 'Extension #6
                                                                                                   time:
                                                                                                  time'
TREC-06
NXMAX
                                                                         'Extension #7 ' time'
'Max NAXIS1 over all extensions'
                                                                                              •
                STRING
                             '2011.02.15-21:48:00-TAI'
                ĹÒNG
                             69Ž
                                                                         'Max NAXIS2 over all extensions'
'Min NAXIS1 over all extensions'
NYMAX
                             425
                LONG
                LÓNG
NXMTN
                             688
                                                                         'Min NAXIS2 over all extensions'
```

Table 2. Sample FITS header of the primary extension (extension 0) and its keywords. The information contained includes the wavelength, the HARP number, the associated NOAA active region number, the central time of each image extension as well as the maximal dimensions of the image data cubes.

<sup>&</sup>lt;sup>1</sup> http://jsoc.stanford.edu/@jsoc/keywords/AIA/AIA02840 K AIA-SDO FITS Keyword Document.pdf

```
XTENSION
                                             STRING
                                                                                  'IMAGE'
                                                                                                                                                                                                              'AIA DATA IMAGE EXTENSION'
BITPIX
NAXIS
NAXIS1
                                              LONG
                                                                                  -32
                                                                                 3
692
                                                                                                                                                                                                               'NUMBER OF DIMENSIONS'
                                              LONG
                                                                                                                                                                                                            'X Pixels'
'Y Pixels'
                                              LONG
 NAXIS2
                                              LONG
LONG
                                                                                  421
                                                                                                                                                                                                              'Samples in time'
NAXIS3
T_REC
                                                                                  11
                                                                                                                                                                                                            '[TAI time]'
'Hours since timeseries start'
'Extension contains valid (1) or no (0) data'
'Valid images out of 11'
                                             STRING
LONG
                                                                                  '2011.02.15_15:48:00_TAI'
 T-IDX
 VALID
                                            LONG
LONG
 NIMVALID
                                                                                                                                                                                                            '[ISO8601] time for image 00', [ISO8601] time for image 01', [ISO8601] time for image 02', [ISO8601] time for image 03', [ISO8601] time for image 04', [ISO8601] time for image 05', [ISO8601] time for image 06', [ISO8601] time for image 07', [ISO8601] time for image 08', [ISO8
                                                                                 '2011-02-15T15:42:02Z'
'2011-02-15T15:43:14Z'
'2011-02-15T15:44:26Z'
 T_IMG00
                                             STRING
STRING
T_IMG01
T_IMG02
                                             STRING
STRING
                                                                                  '2011-02-15T15:45:38Z'
 T_IMG03
T_IMG04
T_IMG05
                                                                                  '2011-02-15T15:46:50Z'
                                             STRING
                                                                                  '2011-02-15T15:48:02Z'
'2011-02-15T15:49:14Z'
                                             STRING
                                             STRING
 T_IMG06
                                                                                                                                                                                                            '[ISO8601] time for image 07'
'[ISO8601] time for image 08'
'[ISO8601] time for image 09'
'[ISO8601] time for image 10'
                                                                                  '2011-02-15T15:50:26Z'
 T_IMG07
                                              STRING
                                                                                  '2011-02-15T15:51:38Z'
'2011-02-15T15:52:50Z'
 T_IMG08
T_IMG09
                                              STRING
                                              STRING
                                                                                  '2011-02-15T15:54:02Z'
'W21S21'
                                             STRING
STRING
T_IMG10
REFHELIO
                                                                                                                                                                                                           '[ISO8601] time for image 10'
'Heliographic pointing string'
'HMI Active Patch number'
'NOAA AR number that best matches this HARP'
'Number of NOAA ARs matching this HARP (0 allowed)'
'List of NOAA ARs matching this HARP'
'[deg] Stonyhurst LAT of flux-weighted cntr pix'
'[deg] Stonyhurst LON of flux-weighted cntr pix'
'[angstrom] Wavelength'
'Wavelength unit: angstrom'
'[time] Pointing reference time'
'[ISO8601] Date when observation started'
'[ISO8601] Observation time'
'[sec] Exposure duration: mean shutter open time'
HARPNUM
                                              LONG
                                                                                 377
11158
 NOAA_AR
                                              LONG
NOAA_NUM
NOAA_ARS
                                              LONG
                                             STRING
                                                                                  <sup>7</sup>11158'
                                                                                  -20.157000
 LAT_FWT
                                              DOUBLE
LON_FWT
WAVELNTH
                                                                                  20.295200
                                             DOUBLE
                                             LONG
                                                                                  211
                                                                                 angstrom'
                                             STRÍNG
 WAVEUNIT
                                                                                  '2011.02.15_15:48:00_TAI'
T_REF
DATE_OBS
                                              STRING
                                                                                  '2011-02-15T15:48:00.62'
                                             STRING
 T_OBS
                                              STRING
                                                                                  '2011-02-15T15:48:02.07Z'
                                                                                                                                                                                                            [Isocour] Observation time
[Isocour] Observ
                                             DOUBLE
 EXPTIME
                                                                                  2.9012420
 EXPSDEV
                                             DOUBLE
                                                                                 0.00020700000
INT_TIME
PIXLUNIT
                                             DOUBLE
                                                                                 3.1562500
'DN'
                                             STRING
                                                                                                                                                                                                          '[DN/electron]'
'AIA_IMG_AEC_DELAY'
'AIA_IMG_AEC_TYPE'
'AIA_IMG_AEC_MODE'
'AIA_IMG_WAVELENGTH'
'X Pixel size in CUNIT1 units'
'Y Pixel size in CUNIT1 units'
'Y pixel units'
'Y pixel units'
'[pix] X location of sun center in CCD'
'[pix] Y location of sun center in CCD'
'[arcsec] X origin - center of the solar disk'
'[deg] Angle between satellite N and solar N'
'[m] Distance from SDO to Sun center'
'[arcsec] of Sun = arcsin(RSUN_REF/DSUN_OBS)'
'[m] Reference radius of Sun'
DN_GAIN
AECDELAY
                                                                                                                                                                                                              '[DN/electron]
                                              DOUBLE
                                                                                 18.300000
                                             LONG
                                                                                  1536
AECTYPE
AECMODE
AIAWVLEN
                                                                                όΟΝ,
                                              LONG
STRING
                                             LONG
                                             DOUBLE
DOUBLE
 CDELT1
                                                                                  0.60000000
                                                                                 0.60000000
 CDELT2
 CUNIT1
                                             STRING
                                                                                  'arcsec', 'arcsec'
 CUNIT2
                                             STRING
DOUBLE
 CRPIX1
                                                                                  -201.50000
 CRPIX2
                                             DOUBLE
                                                                                 622.50000
 CRVAL1
                                             DOUBLE
                                                                                 0.0000000
 CRVAL2
                                             DOUBLE
                                                                                 0.0000000
 CROTA2
                                             DOUBLE
                                                                                 0.0000000
DSUN_OBS
RSUN_OBS
                                                                                1.4773886e+11
971.72022
                                             DOUBLE
                                             DOUBLE
                                                                                                                                                                                                          '[arcsec] of Sun = arcsin(RSUN_REF/DSUN_OBS)'
'[m] Reference radius of Sun'
'[deg] Master pointing CCD rotation wrt SDO Z axis'
'[arcsec/pixel] Master pointing image scale'
'[m/s] Speed of observer in radial direction'
'[m/s] Speed of observer in solar-W direction'
'[m/s] Speed of observer in solar-N direction'
'[arcsec] Ref pixel pointing, arc sec W from sun center'
'[arcsec] Ref pixel pointing, arc sec N from sun center'
                                                                                6.9600000e+08
 RSUN_REF
                                             DOUBLE
INST_ROT
IMSCL_MP
                                             DOUBLE
                                                                                0.056433000
                                                                                0.60075802
-1972.2185
                                             DOUBLE
 OBS_VR
                                             DOUBLE
                                             DOUBLE
                                                                                 28105.801
-1553.5497
 OBS_VW
                                             DOUBLE
DOUBLE
 OBS_VN
 XCEN
                                                                                  328.80002
                                                                                 -246.90001
'degradation performed
using calibration
version 10'
                                             DOUBLE
STRING
 YCEN
 DEGRAD
                                                                                                                                                                                                             'Degradation correction'
 PCOUNT
                                              LONG
 GCOUNT
                                              LONG
                                                                                                                                                                                                            'Type of X image coordinate axis'
'Type of Y image coordinate axis'
                                             STRING
STRING
                                                                                HPLN-TAN
HPLT-TAN
 CTYPE1
 CTYPE2
```

Table 3. Sample FITS header of an image extension.

417

418

419

420

438

439

448

449

450

#### B. DETAILS ON DATA ACQUISITION FOR REMOTE-DRMS SITES

In order to produce the AARP dataset, NWRA made extensive use of being a remote-SUMS/DRMS 410 (Storage Unit Management System/Data Record Management System) site for the SDO mission. As 411 such, NWRA can query, access, and, in some aspects, "mirror" the SDO databases in a manner 412 directly analogous to the host institution (Stanford University) through the Stanford Joint Science 413 Operations Center (JSOC). Many institutions have invested in this capability. To produce this 414 curated dataset required numerous steps and considerations that we describe here, many of which 415 are unique to the SUMS/DRMS system, but some were unexpected, hence worth providing to the 416 community.

We did find this approach most tenable (vs. using the JSOC on-line interfaces including the ssw cutout service.pro, see Appendix C), in part because we could simultaneously process multiple HARP-based AARPs that were often present on the disk, reducing the I/O load and processing time significantly.

Thus, NWRA subscribed to three AIA data series: aia.lev1 (the "data series"), 421 aia.lev1 euv 12s, and aia.lev1 uv 24s (the "header series"). The first queries the actual im-423 422 age data, the latter two query the metadata or header information for EUV (94, 131, 171, 193, 211, 424 304, 335A) and UV (1600, 1700A) wavelengths respectively; the metadata alone, which comes with 425 the subscriptions, is ≈100GB. In order to download and then access a complete image including 426 its header information within the SUMS/DRMS system, both the data and header series must be 427 queried; data within JSOC series are referred to by "prime keys" (often, but not exclusively, a refer-428 ence time such as T REC) then data are selected further by refining keyword searches. From servers 429 hosting a remote-SUMS/DRMS system, querying the SUMS/DRMS database can be done using 430 line show info (http://jsoc.stanford.edu/doxygen\_html/group\_show\_info.html), which 431 is callable from within other codes (e.g. bash, IDL, or Python) and the output used accordingly.

To construct an AARP data set, the needed image data are downloaded first then addi-433 tional queries are constructed in order to access the correct entries in the SUMS/DRMS for 434 analysis. Image data were batch-transferred using the Java Mirroring Daemon (JMD), writ-435 ten and implemented by the National Solar Observatories (http://docs.virtualsolar.org/wiki/jmd; 436 http://vso.tuc.noao.edu/VSO/w/index.php/Main\_Page). Using an example of the 13 m interval cen-437 tered at 15:48:00 UT on 2011.01.01 for 94A, the following steps are taken:

1. For 13 m of data at 72 s cadence (see Section 2.3), the "slot time" or first target image is 15:42:00. This somewhat generic timestamp is not accepted by aia.lev1 series, so the prime keys are obtained by querying the aia.lev1 euv 12 series:

```
keys are obtained by querying the ala.lev1 <u>e</u>uv <u>1</u>2 series:

$ show_info key="T_REC,T_OBS" "aia.lev1 <u>e</u>uv 12s[2011-01-01T15:42:00/13m@72s][?

QUALITY=0 ?][? EXPTIME>1.8 and EXPTIME<3.0 ?][? WAVELNTH=94 ?]"

> T_REC T_OBS

> 2011-01-01T15:42:02Z 2011-01-01T15:42:03.57Z

> 2011-01-01T15:43:14Z 2011-01-01T15:43:15.57Z

> 2011-01-01T15:44:26Z 2011-01-01T15:44:27.57Z

...
```

as T  $\underline{R}EC$  is required for the header series (aia.lev1  $\underline{e}uv$   $\underline{1}2$ ) whereas T  $\underline{O}BS$  is needed for the data series (aia.lev1). Note that we specify not just wavelength and exposure time (to avoid AEC data), but the data-quality requirement as well. In point of fact, we would query e.g.

452

453

454

455

467

468

470

475

476

2011.01.01  $\underline{1}5:42:00/13m@72s$  initially and try e.g. 2011.01.01  $\underline{1}5:41:48/13m@72s$  if fewer than the expected number of records were present, or if the difference between T  $\underline{R}EC$ , T  $\underline{O}BS$  was greater than 18 s. Note that the wavelength can be used in the header series as a second prime key, but not in the data series, so we generally adopted the practice of invoking the keyword request for all.

2. Populate the local aia.lev1 series with the requested full-disk data. To set up the JMD data-transfer request requires the sunum (storage unit unique identifier that is associated with 458 a given data series query) and recnum (a record number corresponding to each record in the 459 storage unit) available from the data series using the prime keys from above:

```
$ show_info -rS key="FSN,T_REC,T_OBS" "aia.lev1[2011-01-01T15:42:03.57Z/13m@72s][?

QUALITY=0 ?][?EXPTIME>1.8 and EXPTIME<3.0?][?WAVELNTH=94?]"

> recnum sunum FSN T_REC T_OBS

> 67456313 190140361 18250728 2011-01-01T15:42:04Z 2011-01-01T15:42:03.57Z

> 67456361 190140436 18250776 2011-01-01T15:43:16Z 2011-01-01T15:43:15.57Z

> 67456409 190140506 18250824 2011-01-01T15:44:28Z 2011-01-01T15:44:27.57Z
```

Note here: there can be more than one record per sunum (depending on the series), the returned T  $\underline{R}EC$  differs from that returned from the header series, and sunum information is not available 469 from the header series.

The Filtergram Sequence Number ("FSN") integers become important later, but can be queried 471 and saved at this step. For each imaging instrument of SDO (e.g. HMI or AIA) the FSN is a 472 unique number for each original image produced by the instrument; we use them to validate the 473 correspondence between the two series. The aia.lev1 series is not designed to accept multiple-474 entry requests ("13m@72s"), and when it fails, the queries must be handled individually.

3. We query for the metadata entries with the new T  $\underline{R}EC$  to confirm the FSN number correspondence:

48. Upon data transfer, we query the data series again, for the location of the files using the FSN numbers returned by the aia <u>lev1 euv 12s</u>. Every remote-SUMS/DRMS system will have its 486 own upper-level structure, but the sunum is consistent between them and is integral to the 487 location:

515

516

517

518

519

520

521

522

523

525

526

527

528

5. We proceed to prepare the data by specifying wavelength, etc. keywords and the file location 494 (e.g., /nwra/SUMS/SUM0/D190140361/S00000). Invoking drot map.pro, degradation, field of 495 view determination and extraction, coalignment, etc., requires numerous additional keyword-496 queries through show info to the hmi.Mharp 720s series. Along the processing, intermediate 497 steps are saved as temporary IDL "idl.sav" files for subsequent assembly into the AARP ex-498 traction FITS files.

The data transfers and referencing were indeed time consuming to automate, as these series are  $_{500}$  constructed with different structure than, e.g. the HMI series. However, having the full-disk data  $_{501}$  locally was key while we formulated the spatial extraction details (see Section 2.2) and the sensitivity  $_{502}$  corrections (see Section 2.1), because we were not required to re-request full-disk data repeatedly as  $_{503}$  the respective approaches were refined.

#### C. NOTES ON USING THE SOLARSOFTWARE CUTOUT SERVICE

Our initial attempt, over 2014-2015, to construct the AARP timeseries HARP-congruent dataset relied on JSOC and its on-line interfaces including through the *Solar SoftWare* IDL package. We used 507 the (SSW Freeland & Handy 1998) tool ssw cutout service.pro written by Sam Freeland at LM-508 SAL. This approach is advantageous for many studies, as the AARP-required data can be downloaded 509 and assembled without the effort and resource allocation necessary to subscribe to the voluminous 510 DRMS series, instead utilizing LMSAL's own subscription. Further, the LMSAL-generated SSW 511 routines are equipped to deal with the subtleties of AIA data processing, such as how to set the 512 cadence to avoid AEC frames.

We automated various steps required to implement the cutout service. Drivers were written specifically to:

- 2. Parse the AIA metadata, and select start/end times to avoid AEC images, getting specified URLs: SSWIDL> ssw isoc time2data, t0, t1, index, urls, /urls only, wave=wave, ds='aia.lev1 euv 12s'
  - 3. Queue AIA cutout exports corresponding to HMI Active Region Patches (HARPs), for the given day using ssw <u>c</u>utout <u>service</u>, invoking the option of an email when the job is complete:

    SSWIDL> ssw <u>c</u>utout <u>service</u>, t0n, t1n, query, stat, ref <u>t</u>ime=tref, fovx=fovxa, fovy=fovya, wave=wavelengths, ref <u>h</u>elio=ref <u>h</u>elio, instrument='aia',aec=0, cadence=cadencestr, description=descr, max <u>f</u>rames=10000, email=email, /RICE
  - 4. Wait for the exports to complete, and move exported FITS files into place
  - 5. Read in the FITS files for each HARP/wavelength/time
- 6. Call aia prep to perform alignment/adjustments on each data cube:
  SSWIDL> aia prep, indexIn, dataIn, index, data, /cutout, index ref=indexIn[refidx]

7. Save the final processed data cubes to FITS (and IDL .sav) files (one per HARP per day)

All of the above steps were automated, initiated by specifying a date. The 94, 131, 171, 193, 211, 304, and 335 Å filter data can be processed together, but the different cadence and data series means 534 the 1600 (UV) must be processed separately.

To produce the full AARP database, however, we came to a few situations that nudged us to the approach in Appendix B. The main failure point stemmed from the (lack of) robustness of data retrieval and needed information not being available to easily detect and validate failures. Data 538 transfer throttling – which can occur on either end of the transfer, and it is not always easy to 539 assess where it occurs – plus "standard-issue network intermittency" often created problems accessing 540 records at the query step. When records then came up absent, it was not straightforward to determine 541 exactly which were missing.

Additionally, the cutout service proved to be slower than expected, primarily due to the need to request data by individual HARPs and individual days, which necessitated repeated full-disk I/O at 544 the host institution when, for example, there were multiple HARPs on the same day and time step. 545 We found significant speed up by internally accessing the full-disk data and performing cutouts *once* 546 for all targets per day and time step.

The ssw cutout service.pro works very well for requests that focus on limited time periods or a small number of targets. It allows for fully customized fields-of-view, significant flexibility on 549 cadence and filter selection, and provides up-to-date pre-processing. Some challenges that were faced 550 during this exploration were beyond the purview of ssw cutout service.pro (e.g. the too-generic 551 JSOC email content). Thus, while the exploration into using the ssw cutout service.pro involved 552 significant investment, it also provided good education and preparation for the switch to relying upon 553 NWRA's remote-DRMS/SUMS subscription (see Appendix B).

NWRA will share ssw cutout service.pro-related driver codes with the community upon request.

# D. PATHOLOGY

531

554

570

571

572

The AIA Active Region Patch (AARP) Database (Dissauer et al. 2022b) follows the HMI Active Region Patch (HARP) definitions (e.g. Hoeksema et al. 2014). By default, all HARPs that were identified between 2010/06 – 2018/12 are included. However, the HARPs include "active pixel" maps 559 within the bounding boxes that are unique to each HARP, even if two (or more) HARP bounding 560 boxes overlap. We do not include the masks (such as are in the hmi.Mharp 720s bitmap.fits 561 segment) as they would only refer, roughly, to the footpoints of the coronal structures. Hence, some 562 AARPs may spatially overlap, or be fully included in one another. We do not remove or try to 563 disentangle these situations as all, but do note that generally the "subsuming" situation is rare and 564 generally for which one of the AARPs is very small.

However, we did find pathological HARPs that needed to be excluded, resulting primarily from periods when the HMI magnetograms were corrupted in such a way as to flag large sections of limb 567 as "active pixels" which then propagated to a HARP definition even though there were otherwise 568 no magnetic concentrations. Of note: the following HARP numbers were removed from the AARP 569 Database:

4276, 4280, 6712, 6713, 6849, 6851, 7207

In addition, HARP 4225 was also initially defined with a corrupted bounding box but in fact there were two NOAA active regions within, although they took up only a small fraction of the original

575

576

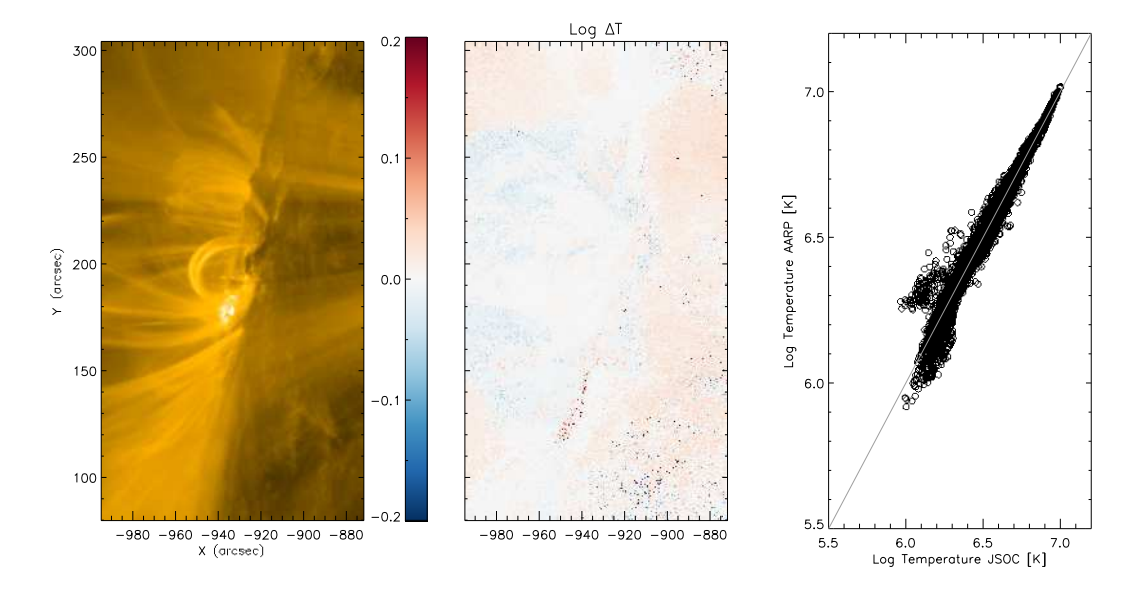


Figure 9. Demonstrating uncertainties in the DEM results using the degradation-corrected AARP dataset to reconstruct temperature, as compared to using the un-corrected JSOC downloaded image files ("ground truth"). Left: 171Å image for context; Middle:  $log(T_{AARP}/T_{JSOC})$  map showing spatial differences between the two; Right: Correlation plot between  $T_{AARP}$  and  $T_{JSOC}$  in log scale. The gray line shows the 1:1 correspondence line.

bounding box. We redefined a HARP-appropriate bounding box according to the active pixel masks 574 (hmi.Mharp 720s bitmap.fits segment, see Hoeksema et al. (2014)), and then extended that FOV as per described in Section 2.2 for inclusion in the AARP database.

# E. DIFFERENTIAL EMISSION MEASURE VALIDATION

The AARP data set is corrected for instrument degradation. In general, we use the DEM code by Cheung et al. (2015) to calculate emission measure, temperature and density maps (Dissauer et al. 579 2022a). By definition, this particular DEM code handles instrument degradation by correcting the 580 temperature response functions returned from aia get response.pro using the image observation 581 times.

Here, we demonstrate that the DEM calculation using the AARP dataset as input, and turning "off" the degradation correction, provides similar results as using the original JSOC output where  $_{584}$  the degradation has not yet been performed and allowing the DEM code to make these corrections  $_{585}$  (Figure 9). The differences are displayed as both spatial maps and a correlation plot, and do not  $_{586}$  exceed the [-0.1,0.1] range in a pixel-by-pixel comparison. This error range is in agreement with  $_{587}$  uncertainties for the sparse solution of Cheung et al. (2015) when compared to a "ground truth" (c.f.,  $_{588}$  their Figures 2 & 3).

Facilities: SDO (HMI and AIA); GOES (XRS)
Software: SolarSoft (Freeland & Handy 1998)

### REFERENCES

```
Abramenko, V. I. 2005, ApJ, 629, 1141,
593 Aggarwal, A., Schanche, N., Reeves, K. K.,
594 Kempton, D., & Angryk, R. 2018, ApJS, 236,
595 15, doi: 10.3847/1538-4365/aab77f
```

```
Al-Ghraibah, A., Boucheron, L. E., & McAteer,
                                                              Golding, T. P., Leenaarts, J., & Carlsson, M.
596
                                                         644
      R. T. J. 2015, A&A, 579, A64,
                                                                2017, A&A, 597, A102,
                                                         645
597
                                                                doi: 10.1051/0004-6361/201629462
      doi: 10.1051/0004-6361/201525978
                                                         646
598
    Alipour, N., Mohammadi, F., & Safari, H. 2019,
                                                              Hagyard, M. J., Smith, J. B. J., Teuber, D., &
                                                         647
599
      ApJS, 243, 20, doi: 10.3847/1538-4365/ab289b
                                                                West, E. A. 1984, SoPh, 91, 115
                                                         648
600
                                                             Harra, L. K., Matthews, S., Culhane, J. L., et al.
    Bamba, Y., Kusano, K., Imada, S., & Iida, Y.
                                                         649
601
      2014, PASJ, 66, S16, doi: 10.1093/pasj/psu091
                                                                2013, ApJ, 774, 122,
                                                         650
602
                                                                doi: 10.1088/0004-637X/774/2/122
    Barnes, G. 2007, ApJL, 670, L53,
                                                         651
603
                                                              Hoeksema, J. T., Liu, Y., Hayashi, K., et al. 2014,
                                                         652
      doi: 10.1086/524107
604
                                                                SoPh, 289, 3483,
                                                         653
    Barnes, G., & Leka, K. D. 2006, ApJ, 646, 1303,
605
                                                                doi: 10.1007/s11207-014-0516-8
                                                         654
      doi: 10.1086/504960
606
                                                             Imada, S., Bamba, Y., & Kusano, K. 2014, PASJ,
                                                         655
    Barnes, W. T., Cheung, M. C. M., Bobra, M. G.,
607
                                                                66, S17, doi: 10.1093/pasj/psu092
                                                         656
      et al. 2020, Journal of Open Source Software, 5,
608
                                                             Inoue, S., Kusano, K., Büchner, J., & Skála, J.
                                                         657
      2801, doi: 10.21105/joss.02801
609
                                                                2018, Nature Communications, 9, 174,
                                                         658
    Bobra, M. G., & Couvidat, S. 2015, ApJ, 798,
610
                                                                doi: 10.1038/s41467-017-02616-8
                                                         659
      135, doi: 10.1088/0004-637X/798/2/135
611
                                                              Ishiguro, N., & Kusano, K. 2017, ApJ, 843, 101,
                                                         660
    Bobra, M. G., Sun, X., Hoeksema, J. T., et al.
612
                                                                doi: 10.3847/1538-4357/aa799b
                                                         661
      2014, SoPh, 289, 3549,
613
                                                             Jonas, E., Bobra, M., Shankar, V., Todd
                                                         662
      doi: 10.1007/s11207-014-0529-3
614
                                                                Hoeksema, J., & Recht, B. 2018, SoPh, 293,
                                                         663
    Bornmann, P. L., & Shaw, D. 1994, SoPh, 150,
615
                                                                #48, doi: 10.1007/s11207-018-1258-9
                                                         664
      127, doi: 10.1007/BF00712882
616
                                                             Joshi, B., Veronig, A. M., Lee, J., et al. 2011, ApJ,
                                                         665
    Braun, D. C. 2016, ApJ, 819, 106,
617
                                                                743, 195, doi: 10.1088/0004-637X/743/2/195
                                                         666
      doi: 10.3847/0004-637X/819/2/106
618
                                                              Komm, R., Ferguson, R., Hill, F., Barnes, G., &
                                                         667
    Canfield, R. C., Priest, E. R., & Rust, D. M. 1975,
619
                                                                Leka, K. D. 2011, SoPh, 268, 389,
                                                         668
      NASA STI/Recon Technical Report N, 76, 361
620
                                                                doi: 10.1007/s11207-010-9552-1
                                                         669
    Centeno, R., Schou, J., Hayashi, K., et al. 2014,
621
                                                             Kontogiannis, I., Georgoulis, M. K., Guerra, J. A.,
                                                         670
      SoPh, 289, 3531,
622
                                                                Park, S.-H., & Bloomfield, D. S. 2019, SoPh,
                                                         671
      doi: 10.1007/s11207-014-0497-7
623
                                                                294, 130, doi: 10.1007/s11207-019-1523-6
                                                         672
    Cheung, M. C. M., Boerner, P., Schrijver, C. J.,
624
                                                             Korsós, M. B., Baranyi, T., & Ludmány, A. 2014,
                                                         673
      et al. 2015, ApJ, 807, 143,
625
                                                                ApJ, 789, 107,
                                                         674
      doi: 10.1088/0004-637X/807/2/143
626
                                                                doi: 10.1088/0004-637X/789/2/107
                                                         675
    Cho, K., Lee, J., Chae, J., et al. 2016, SoPh, 291,
627
                                                             Krall, K. R., Smith, Jr., J. B., Hagyard, M. J.,
                                                         676
      2391, doi: 10.1007/s11207-016-0963-5
628
                                                                West, E. A., & Cummings, N. P. 1982, SoPh,
                                                         677
    Del Zanna, G. 2013, A&A, 558, A73,
629
                                                                79, 59, doi: 10.1007/BF00146973
                                                         678
      doi: 10.1051/0004-6361/201321653
630
                                                              Kusano, K., Iju, T., Bamba, Y., & Inoue, S. 2020,
    Dissauer, K., Leka, K. D., Barnes, G., & Wagner,
631
                                                                Science, 369, 587, doi: 10.1126/science.aaz2511
                                                         680
      E. L. 2022a, ApJ, in preparation
632
                                                             Leamon, R. J., McIntosh, S. W., & Title, A. M.
    Dissauer, K., Leka, K. D., & Wagner, E. L. 2022b,
633
                                                                2022, Frontiers in Astronomy and Space
                                                         682
      The NWRA AIA Active Region Patch
634
                                                                Sciences, 9, 886670,
                                                         683
      Database, V1, doi: TBD
635
                                                                doi: 10.3389/fspas.2022.886670
                                                         684
    Freeland, S. L., & Handy, B. N. 1998, SoPh, 182,
                                                              Leka, K. D., & Barnes, G. 2003a, ApJ, 595, 1277
636
      497, doi: 10.1023/A:1005038224881
                                                              —. 2003b, ApJ, 595, 1296
637
    Galvez, R., Fouhey, D. F., Jin, M., et al. 2019,
                                                              -. 2007, ApJ, 656, 1173, doi: 10.1086/510282
638
                                                         687
      ApJS, 242, 7, doi: 10.3847/1538-4365/ab1005
                                                             Leka, K. D., Barnes, G., & Wagner, E. L. 2018,
639
                                                         688
    Georgoulis, M. K. 2012, SoPh, 276, 161,
                                                                Journal of Space Weather and Space Climate, 8,
640
                                                         689
      doi: 10.1007/s11207-010-9705-2
                                                                A25, doi: 10.1051/swsc/2018004
641
                                                         690
    Georgoulis, M. K., & Rust, D. M. 2007, ApJL,
                                                              Leka, K. D., Dissauer, K., Barnes, G., & Wagner,
642
                                                         691
      661, L109, doi: 10.1086/518718
                                                                E. L. 2022, ApJ, accepted
643
                                                         692
```

```
Lemen, J. R., Title, A. M., Akin, D. J., et al. 2012,
693
      SoPh, 275, 17, doi: 10.1007/s11207-011-9776-8
694
    Li, J., Mickey, D. L., & LaBonte, B. J. 2005, ApJ,
695
      620, 1092, doi: 10.1086/427205
696
    Mango, S. A., Bohlin, J. D., Glackin, D. L., &
697
      Linsky, J. L. 1978, ApJ, 220, 683,
698
      doi: 10.1086/155952
699
    Mason, J. P., & Hoeksema, J. T. 2010, ApJ, 723,
700
      634, doi: 10.1088/0004-637X/723/1/634
701
    McAteer, R. T. J., Gallagher, P. T., & Ireland, J.
702
      2005, ApJ, 631, 628, doi: 10.1086/432412
703
    McIntosh, P. S. 1990, SoPh, 125, 251
704
    Nishizuka, N., Sugiura, K., Kubo, Y., et al. 2017,
705
      ApJ, 835, 156,
706
      doi: 10.3847/1538-4357/835/2/156
707
    O'Dwyer, B., Del Zanna, G., Mason, H. E.,
708
      Weber, M. A., & Tripathi, D. 2010, A&A, 521,
709
      A21, doi: 10.1051/0004-6361/201014872
710
    Park, S.-H., Guerra, J. A., Gallagher, P. T.,
711
      Georgoulis, M. K., & Bloomfield, D. S. 2018,
712
      SoPh, 293, 114, doi: 10.1007/s11207-018-1336-z
713
    Park, S.-H., Leka, K. D., & Kusano, K. 2021, ApJ,
714
      911 press, 79, doi: 10.3847/1538-4357/abea13
715
    Pesnell, W. D., Thompson, B. J., & Chamberlin,
716
      P. C. 2012, SoPh, 275, 3,
717
      doi: 10.1007/s11207-011-9841-3
718
    Qiu, J., & Cheng, J. 2017, ApJL, 838, L6,
719
      doi: 10.3847/2041-8213/aa6798
720
    Reinard, A. A., Henthorn, J., Komm, R., & Hill,
721
      F. 2010, ApJL, 710, L121,
722
      doi: 10.1088/2041-8205
723
    Sawyer, C., Warwick, J. W., & Dennett, J. T.
724
      1986, Solar Flare Prediction (Boulder, CO:
725
      Colorado Assoc. Univ. Press)
726
    Scherrer, P. H., Schou, J., Bush, R. I., et al. 2012,
727
      SoPh, 275, 207, doi: 10.1007/s11207-011-9834-2
728
    Schonfeld, S. J., White, S. M., Hock-Mysliwiec,
729
      R. A., & McAteer, R. T. J. 2017, ApJ, 844, 163,
730
      doi: 10.3847/1538-4357/aa7b35
731
    Schou, J., Scherrer, P. H., Bush, R. I., et al. 2012,
732
      SoPh, 275, 229, doi: 10.1007/s11207-011-9842-2
733
    Seki, D., Otsuji, K., Isobe, H., et al. 2017, ApJL,
734
      843, L24, doi: 10.3847/2041-8213/aa7559
735
```

```
SILSO World Data Center. 2010-2018,
      International Sunspot Number Monthly
      Bulletin and online catalogue
738
    Smith, J. B. J., Neidig, D. F., Wiborg, P. H.,
      et al. 1996, in ASP Conference Ser., Vol. 95,
740
      Solar Drivers of Interplanetary and Terrestrial
741
      Disturbance, 54-65
742
    Sterling, A. C., & Moore, R. L. 2001, ApJ, 560,
743
      1045, doi: 10.1086/322241
744
    Sterling, A. C., Moore, R. L., & Freeland, S. L.
745
      2011, ApJL, 731, L3,
746
      doi: 10.1088/2041-8205/731/1/L3
747
    Thiemann, E. M. B., Chamberlin, P. C., Eparvier,
748
      F. G., & Epp, L. 2018, SoPh, 293, 19,
749
      doi: 10.1007/s11207-018-1244-2
750
    Thompson, W. T. 2006, A&A, 449, 791,
751
      doi: 10.1051/0004-6361:20054262
752
    Threlfall, J., Neukirch, T., & Parnell, C. E. 2017,
753
      SoPh, 292, 45, doi: 10.1007/s11207-017-1060-0
754
    Ugarte-Urra, I., Warren, H. P., Upton, L. A., &
755
      Young, P. R. 2017, ApJ, 846, 165,
756
      doi: 10.3847/1538-4357/aa8597
757
    Wang, J., Shi, Z., Wang, H., & Lü, Y. 1996, ApJ,
758
      456, 861
759
    Warren, H. P., Winebarger, A. R., & Brooks,
760
      D. H. 2012, ApJ, 759, 141,
761
      doi: 10.1088/0004-637X/759/2/141
762
    Welsch, B. T., Li, Y., Schuck, P. W., & Fisher,
763
      G. H. 2009, ApJ, 705, 821,
764
      doi: 10.1088/0004-637X/705/1/821
765
    Woods, M. M., Harra, L. K., Matthews, S. A.,
766
      et al. 2017, SoPh, 292, 38,
767
      doi: 10.1007/s11207-017-1064-9
768
    Worden, J., Woods, T. N., Neupert, W. M., &
769
      Delaboudinière, J.-P. 1999, ApJ, 511, 965,
770
      doi: 10.1086/306693
771
    Zhang, Q. M., Su, Y. N., & Ji, H. S. 2017, A&A,
      598, A3, doi: 10.1051/0004-6361/201629477
773
    Zirin, H., & Liggett, M. 1987, SoPh, 113, 267
774
    Zirin, H., & Marquette, W. 1991, SoPh, 131, 149,
775
      doi: 10.1007/BF00151751
776
   Zirin, H., & Tanaka, K. 1973, SoPh, 32, 173
```